

Laser Chirp Linearization and Phase Noise Compensation for Frequency-modulated Continuous-wave LiDAR

Xiaosheng Zhang



Electrical Engineering and Computer Sciences
University of California, Berkeley

Technical Report No. UCB/EECS-2021-9

<http://www2.eecs.berkeley.edu/Pubs/TechRpts/2021/EECS-2021-9.html>

April 4, 2021

Copyright © 2021, by the author(s).
All rights reserved.

Permission to make digital or hard copies of all or part of this work for personal or classroom use is granted without fee provided that copies are not made or distributed for profit or commercial advantage and that copies bear this notice and the full citation on the first page. To copy otherwise, to republish, to post on servers or to redistribute to lists, requires prior specific permission.

**Laser Chirp Linearization and Phase Noise Compensation for
Frequency-modulated Continuous-wave LiDAR**

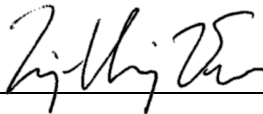
by Xiaosheng Zhang

Research Project

Submitted to the Department of Electrical Engineering and Computer Sciences,
University of California at Berkeley, in partial satisfaction of the requirements for the
degree of **Master of Science, Plan II**.

Approval for the Report and Comprehensive Examination:

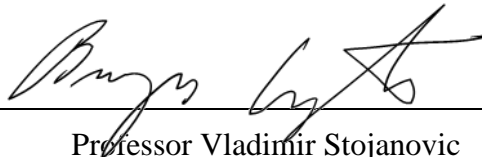
Committee:



Professor Ming C. Wu
Research Advisor

4/3/2021

(Date)



Professor Vladimir Stojanovic
Second Reader

4/2/21

(Date)

Abstract

Laser Chirp Linearization and Phase Noise Compensation for Frequency-modulated Continuous-wave LiDAR

by

Xiaosheng Zhang

Master of Science in Electrical Engineering and Computer Sciences

University of California, Berkeley

Professor Ming C. Wu, Chair

Light detection and ranging (LiDAR) is the enabling sensor for high-resolution three-dimensional (3D) imaging. It has been widely used in scientific research, industrial metrology, robotics, autonomous vehicles, and consumer electronics. Compared with the conventional pulsed time-of-flight LiDAR, the frequency-modulated continuous-wave (FMCW) LiDAR requires lower optical power, lower electronic bandwidth, and is intrinsically immune to the interference from the ambient light and other LiDAR units due to the coherent detection mechanism. However, an FMCW LiDAR typically requires a linearly frequency-chirped laser with low phase noise, which are conventionally realized by complicated feedback control circuits. In this work, we report on linearizing the laser chirp by the iterative learning pre-distortion method and compensating for the phase noise by processing the signal with the help of a monitor interferometer. Experimental results with a commercial distributed feedback (DFB) laser show that with the pre-distortion linearization method, the relative residual nonlinearity of the laser chirp can be reduced to less than 0.003%, and the post-processing phase noise compensation can extend the LiDAR detection range to more than 250 m. With the proposed methods, high-performance and low-cost FMCW LiDAR systems can be achieved without requiring expensive narrow-linewidth lasers or complex controllers.

Table of Content

1. Introduction.....	1
1.1 Background.....	1
1.2 FMCW LiDAR principle	3
1.3 Laser chirp nonlinearity in an FMCW LiDAR.....	4
2. Laser chirp linearization by iterative learning pre-distortion	6
2.1 Principle and setup.....	6
2.2 Experimental results.....	8
3. Phase noise compensation process.....	12
3.1 Principle and setup.....	12
3.2 Experimental results.....	17
4. Conclusions.....	20
5. Funding and Acknowledgements.....	21
6. References.....	22

1. Introduction

1.1 Background

Three-dimensional (3D) sensors that measure the 3D coordinates of surfaces and objects enable machines to observe and perceive the surroundings. They have been widely used in automobiles, robots, unmanned aerial vehicles, and consumer electronics. Typical 3D sensing methods include camera-based stereo vision [1] and structured light [2], radio detection and ranging (Radar) [3], ultrasonic ranging [4], and light detection and ranging (LiDAR) [5]. Compared with other methods, LiDAR has higher resolutions in both longitudinal and lateral directions in a long range thanks to the short wavelength and low divergence of the laser beam. In addition, LiDAR is capable to work in dark environments and provide reflectivity and velocity information of the objects.

A schematic of a typical LiDAR system is shown in Figure 1.1. A laser beam is emitted towards the object at a distance D via the transmitter, and the reflected or scattered light from the object is collected by the receiver and the photodetector. The transmitter and receiver may share the same optical aperture (monostatic configuration) or have separate apertures (bistatic configuration, as shown in Figure 1.1). To collect the 3D information of the entire scene, a beam scanner may be implemented to direct the beam towards different points on the object sequentially, or a detector array may be used to receive the light coming back from multiple points on the object in parallel.

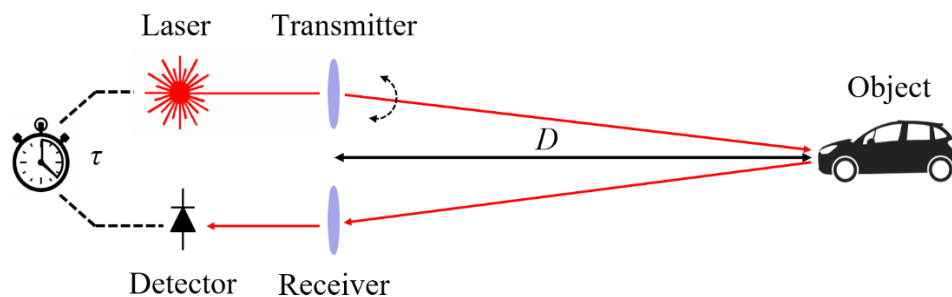


Figure 1.1. Schematic of a typical LiDAR system in the bistatic configuration.

The LiDAR measures the round-trip time τ of the light traveling between itself and the object and computes the distance by $D = c\tau/2$, where c is the speed of light, which is

defined as a constant in the vacuum. The speed of light in the air is slower than in the vacuum by approximately 0.3%, depending on atmospheric parameters such as temperature, pressure, and humidity [6]. In a practical LiDAR, the speed of light can either be calculated from the atmospheric conditions or simply be approximated using the vacuum value according to the required accuracy.

The round-trip time τ can be measured by several methods, and the most common ones are pulsed time-of-flight (ToF), amplitude-modulated continuous-wave (AMCW), and frequency-modulated continuous-wave (FMCW) [5]. The pulsed ToF LiDAR emits a laser pulse towards the object, and τ is directly counted by electronics triggered by the transmitted and received pulses. It has a simple optical setup and is good at measuring a long distance. However, the timing electronics need to be high-speed to achieve a high ranging resolution. The short laser pulse with a high peak power may be problematic for integrated photonics platforms. Besides, optical pulses emitted from other LiDAR transmitters may cause false detections.

In an AMCW LiDAR, the round-trip time τ is converted to the envelope phase delay of an amplitude-modulated light. AMCW LiDAR is able to achieve a high resolution for a short distance without high-speed electronics, and can be implemented with a regular continuous-wave laser. However, with a single modulation frequency, there is a trade-off between the detection range and resolution, which may be solved by measuring the same object with several different modulation frequencies. The light intensity variations caused by the object surface properties or the light propagation path instability can also introduce ranging errors.

In an FMCW LiDAR, the round-trip time τ is converted to the optical frequency change of a frequency-modulated light. Different from the previous two methods, FMCW LiDAR employs the coherent detection mechanism where the light from two paths interferes with each other, thus requires lower optical power and is intrinsically immune to other LiDAR transmitters and the ambient light. It can also detect the Doppler frequency shift from a moving object and measure its velocity. However, FMCW LiDAR

has strict requirements on the chirp linearity and the phase noise of the light source, which will be discussed in the following sections.

1.2 FMCW LiDAR principle

Figure 1.2(a) shows a schematic of an FMCW LiDAR. The optical frequency of a continuous-wave laser is modulated in a triangular wave fashion. The light is split into a reference path with a fixed length as the local oscillator, and a probe path traveling towards and back from the object at a distance D . The round-trip time is thus $\tau = 2D/c$. The two paths are mixed at a photodetector, generating a radio-frequency beat note with a frequency f_b equal to the optical frequency difference, which can be measured by frequency analysis methods such as a Fourier Transform (FT).

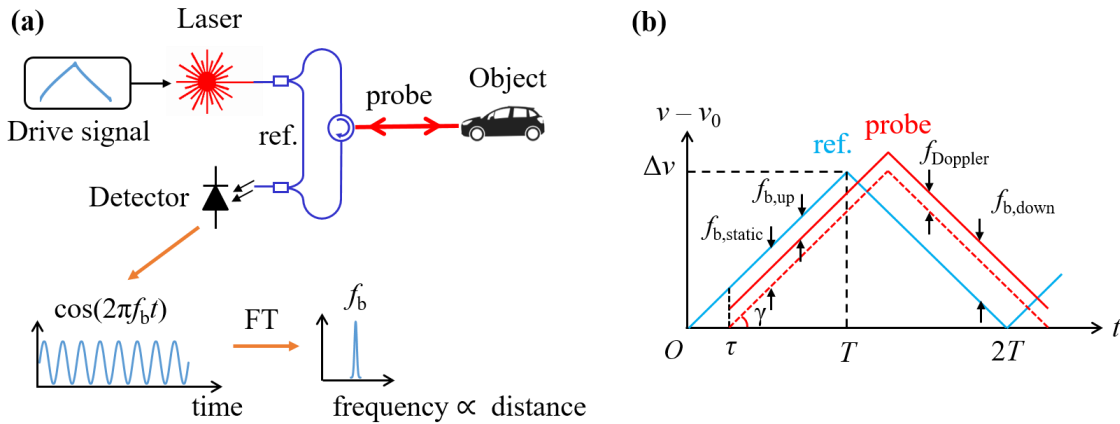


Figure 1.2. (a) Schematic of an FMCW LiDAR. (b) Laser frequency as a function of time in the reference and probe paths of an FMCW LiDAR.

The blue curve in Figure 1.2(b) shows the optical frequency ν as a function of time t in the reference path, assuming the initial optical frequency is ν_0 , the periods for the up-chirp and the down-chirp are both T , and the maximum frequency excursion is $\Delta\nu = \gamma T$. If the object and LiDAR are relatively stationary, the optical frequency curve in the probe arm will be the same as in the reference arm except for a time delay τ , shown as the dashed red curve in Figure 1.2(b). The optical frequency difference between the two paths is $f_{b,\text{static}} = \gamma\tau = 2D\gamma/c$, therefore the object distance is $D = cf_{b,\text{static}}/2\gamma$. If $f_{b,\text{static}}$ is

measured by a Fourier Transform of the beat signal with a period T , its resolution is $\delta f_b = 1/T$, thus the bandwidth-limited distance resolution is [7]

$$\delta D = c\delta f_b/2\gamma = c/2\gamma T = c/2\Delta v. \quad (1.1)$$

An object moving towards the LiDAR with a radial velocity V will cause a Doppler frequency shift $f_D = 2V/\lambda$ in the optical frequency of the probe path (shown as the solid red curve in Figure 1.2(b)), where λ is the wavelength of the light. The static beat frequency and the Doppler shift can be computed by summing and subtracting the beat frequencies of the up-chirp and down-chirp, i.e. $f_{b,\text{static}} = (f_{b,\text{up}} + f_{b,\text{down}})/2$, and $f_{\text{Doppler}} = (f_{b,\text{down}} - f_{b,\text{up}})/2$, so the object distance and velocity can be measured at the same time, i.e.

$$D = cf_{b,\text{static}}/2\gamma = c(f_{b,\text{up}} + f_{b,\text{down}})/4\gamma, \quad (1.2)$$

$$V = \lambda f_D/2 = \lambda(f_{b,\text{down}} - f_{b,\text{up}})/4. \quad (1.3)$$

1.3 Laser chirp nonlinearity in an FMCW LiDAR

In the previous section, we assumed a linear laser chirp $\nu(t) = \nu_0 + \gamma t$. However, the chirp is never ideally linear in reality. We represent the chirp nonlinearity as $\nu_{\text{nl}}(t)$ so the actual laser chirp is $\nu(t) = \nu_0 + \gamma t + \nu_{\text{nl}}(t)$. This will result in a varying beat frequency $f_b(t) = \nu(t) - \nu(t - \tau) = \gamma\tau + [\nu_{\text{nl}}(t) - \nu_{\text{nl}}(t - \tau)]$, thus degrading the frequency resolution δf_b and the distance resolution δD . We have shown in [8] that by applying the Carson bandwidth rule [9], the frequency resolution can be estimated by

$$\delta f_b = (1 + 2\pi\tau\nu_{\text{nl,rms}})/T, \quad (1.4)$$

and the distance resolution can be estimated by

$$\delta D = c(1 + 2\pi\tau\nu_{\text{nl,rms}})/(2\Delta v), \quad (1.5)$$

where $\nu_{\text{nl,rms}}$ represents the root mean square (RMS) value of $\nu_{\text{nl}}(t)$ in the chirp period T . The resolution is higher with a smaller $\nu_{\text{nl,rms}}$, and when the chirp nonlinearity is negligible, i.e. $2\pi\tau\nu_{\text{nl,rms}} \ll 1$, Equation (1.5) will reduce to the bandwidth-limited resolution in Equation (1.1). The nonlinearity effects also depend on the round-trip time τ , and a longer object distance will result in a lower resolution for the same $\nu_{\text{nl,rms}}$. The

relative chirp nonlinearity can also be represented by the linear regression coefficient of determination $r^2 = 1 - 12(v_{nl,rms}/\Delta v)^2$ [8].

In general, the sources of the chirp nonlinearity can be classified into two categories, namely systematic nonlinearity and random nonlinearity. The systematic nonlinearity is the repetitive nonlinearity typically due to the nonlinear dynamic response of the laser, i.e. a linear drive waveform will result in a nonlinear chirp. The systematic nonlinearity can be characterized and compensated for in advance, for example, the laser can be driven with a proper pre-distorted waveform that leads to a linear chirp, and this waveform will not change if the laser dynamics remain the same.

The random nonlinearity comes from random noise sources such as the laser spontaneous emission, the drive current shot noise, the thermal fluctuation, etc. These random noise sources together affect the frequency or phase stability of the laser, thus can be combined as the laser phase noise. A high level of phase noise degrades the laser coherence, resulting in a short laser coherent time, a short coherent length, and a wide linewidth [10]. It is worth to note that a laser being frequency chirped may have higher phase noise than it under a constant drive current [11].

An ideal laser for FMCW LiDAR should have a linear chirp given a linear drive waveform (no systematic nonlinearity) and a low phase noise (low random nonlinearity, or a narrow linewidth). The chirp nonlinearity in an FMCW LiDAR is conventionally reduced by two methods. The first is active control of the laser frequency using optical phase-locked loops [12]. This method provides precise control of the laser chirp and suppresses the phase noise, but requires complex electronic circuits with high bandwidths. The other method is resampling the measured beat signal at non-uniformly distributed time points according to the nonlinear laser chirp measured by a monitor interferometer [13]. This post-processing method can be easily implemented, but the computational cost is heavy due to the interpolation operation, and the Doppler shift information can be destroyed by the non-uniform resampling.

In this work, we propose to compensate for the two types of chirp nonlinearity by two steps. At the first step, a pre-distorted laser drive waveform is obtained by the iterative

learning control (ILC) method to reduce the systematic nonlinearity. Once the ILC pre-distortion process is completed, the laser can be driven by the fixed pre-distorted drive waveform without real-time corrections. The nonlinearity can be reduced so that at a short to medium distance (for example tens of meters) the resolution given in Equation (1.5) falls in the bandwidth-limited region and the second step nonlinearity compensation may even become unnecessary. This method can be easily implemented on an FMCW LiDAR with any type of laser, and it does not require any active control or additional post-processing.

At a long distance (for example hundreds of meters), the random nonlinearity effects will become more significant. At the second step, the laser chirp is measured by a monitor interferometer and the nonlinearity is compensated for in post-processing. Different from the resampling method, the proposed processing method does not require interpolation operation thus can be computed faster, and it does not affect the Doppler shift information. These two steps will be discussed in detail in sections 2 and 3 respectively.

2. Laser chirp linearization by iterative learning pre-distortion

2.1 Principle and setup

To compensate for the systematic laser chirp nonlinearity due to the nonlinear laser dynamics, i.e. a linear drive waveform resulting in a nonlinear laser chirp, we can find a proper pre-distorted drive waveform that leads to the desired linear chirp. Conventionally, the relation between the drive waveform and the laser chirp is first approximated by a model, such as the linear time-invariant model [14], the current-dependent gain model [15], and the power function model [16]. The model parameters are then obtained by experimental results, and the pre-distorted drive waveform is solved from the model. However, an analytical model cannot perfectly describe the laser behavior and thus has intrinsic errors. On the other hand, the iterative learning control (ILC) method is able to achieve a proper pre-distorted waveform for a repetitive dynamic

system without requiring any model, thus eliminating the model errors. It has been applied to many areas and is very suitable for laser chirp linearization [17].

A schematic of the ILC pre-distortion for laser chirp linearization is shown in Figure 2.1. The process starts with an initial laser drive waveform $u_1(t)$ and iteratively updates the drive waveform $u_k(t)$ at the k^{th} iteration until a pre-distorted waveform $u_d(t)$ that leads to the desired linear chirp $v_d(t)$ is achieved. In each iteration, the actual laser chirp $v_k(t)$ is measured and compared with $v_d(t)$, the error $e_k(t) = v_d(t) - v_k(t)$ is computed, and the drive waveform for the next iteration $u_{k+1}(t)$ is updated from $e_k(t)$ and $u_k(t)$ by the waveform update algorithm. The iteration stops when the error $e_k(t)$ is smaller than a preset value or when $e_k(t)$ stops decreasing. In this work, a triangular drive waveform is used as $u_1(t)$ since there is no prior knowledge of the laser dynamics, but the process will converge faster if $u_1(t)$ is closer to $u_d(t)$. In addition, we use the linear update algorithm $u_{k+1}(t) = u_k(t) + p \cdot e_k(t)$ where p is a constant, which has been proven to make $v_k(t)$ converge to $v_d(t)$ with a sufficiently small p [18]. Other more sophisticated algorithms may help increase the converging speed.

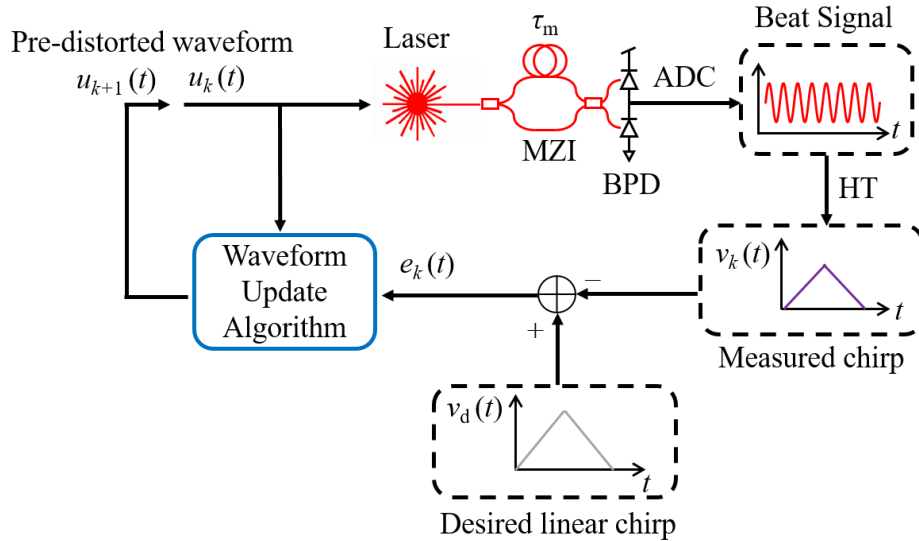


Figure 2.1. Schematic of the ILC pre-distortion for laser chirp linearization.

To measure the laser chirp $v_k(t)$, the light is sent into a monitor Mach-Zehnder Interferometer (MZI) with a constant time delay τ_m and detected by a pair of balanced

photodetectors. The beat frequency is thus $f_{b,k}(t) = \nu_k(t) - \nu_k(t - \tau_m)$, and can be approximated by the first term in its Taylor Series $f_{b,k}(t) = \nu_k'(t)\tau_m$ when τ_m is significantly smaller than the chirp period T . The phase of the beat signal, which can be extracted by applying a Hilbert Transform (HT) to the beat signal, is thus $\varphi_{b,k}(t) = 2\pi\tau_m \int \nu_k'(t) dt = 2\pi\tau_m \nu_k(t)$. Therefore, the laser chirp can be computed by $\nu_k(t) = \varphi_{b,k}(t)/2\pi\tau_m$.

The ILC pre-distortion method does not require any knowledge of the laser dynamics so it can be applied to any types of laser sources. Once the pre-distorted waveform $u_d(t)$ is achieved, the laser is then driven by this fixed waveform for future LiDAR measurements, without any active control or additional post-processing. Changes of the laser dynamics due to external environment variations or internal laser aging may gradually degrade the chirp linearity thus require restarting the ILC pre-distortion process to update the pre-distorted waveform. However, this recalibration process will start from the previously obtained pre-distorted waveform instead of a triangular waveform, therefore can be very fast to complete. In addition, modern semiconductor lasers are usually integrated with a thermoelectric cooler (TEC) that helps prevent linearity degradation due to external temperature fluctuations.

2.2 Experimental results

The ILC pre-distortion linearization is experimentally tested on a commercial distributed feedback (DFB) laser (DFB-1550, Optilab). The DFB laser is 200 mA DC biased and modulated by a current waveform with a 140 mA peak-to-peak value at 4 kHz rate (chirp period $T = 125 \mu\text{s}$) produced by an arbitrary waveform generator (AWG) (33250A, Keysight Technologies). The central wavelength of the laser is 1550 nm, and the chirp excursion is approximately 36 GHz. The monitor MZI has a delay $\tau_m = 5 \text{ ns}$. The beat signal is detected by a pair of balanced photodetectors (PDB450C-AC, Thorlabs) and recorded by an analog-to-digital converter (ADC) (PXIe-5114, National Instruments) at 125M samples per second. The data processing and instrument control are performed on a laptop computer. At each iteration, the laser chirp data is averaged over 1000 measurements to reduce noise. The laser drive waveform is down-sampled to 10M

samples per second when transferred to the AWG due to the data length and transfer time limitation. The laser chirp around the up and down-chirp transition cannot be perfectly linearized because of the limited slew rate and bandwidth of the AWG, so the central 100 μs period in each chirp (80% of the 125 μs chirp) is selected as the region of interest (ROI) for linearity evaluation and LiDAR measurements.

Figure 2.2 shows the experimental results of the ILC pre-distortion linearization on the DFB laser. At each iteration, the linear regression coefficient of determination r of the up and down-chirps is computed by applying a least-squares linear fitting to the measured laser chirp, and $(1 - r^2)$ is plotted in Figure 2.2(a) showing the ILC pre-distortion process gradually decreasing the laser chirp linearity. The laser chirps and the residual nonlinearity in the ROIs at the 1st iteration and the 14th iteration are shown in Figures 2.2(b), (c), (e), and (f) respectively. The chirp nonlinearity $v_{\text{nl,rms}}$ is reduced by about 600x from 863 MHz to 1.4 MHz (relative nonlinearity 0.004%) in the down-chirp, and reduced by 140x from 140 MHz to 1.0 MHz (relative nonlinearity 0.003%) in the up-chirp. According to Equation (1.5), bandwidth-limited resolution can be achieved at an object distance up to 24 m with the 1.0 MHz residual nonlinearity. Figure 2.2(d) shows the pre-distorted laser modulation waveform at the 14th iteration.

The p coefficient in the linear update algorithm $u_{k+1}(t) = u_k(t) + p \cdot e_k(t)$ affects the convergence and speed of the ILC pre-distortion process. A smaller p coefficient ensures that $v_k(t)$ converges to $v_d(t)$, but also decreases the convergence speed. Figure 2.3 shows the convergence speed of the ILC pre-distortion process with different p coefficients when linearizing the up-chirp of the DFB laser. Here $e_k(t)$ and $u_k(t)$ are normalized by the total frequency excursion and the drive waveform amplitude respectively, so p is a dimensionless number. The ILC pre-distortion process converges significantly faster when p is increased from 0.1 to 1.5. However, the process becomes unstable when p is increased over 2.5. The results suggest that with an optimized p value, the linear update algorithm is able to achieve good chirp linearity with fewer than 10 iterations, which can be completed within only tens of seconds.

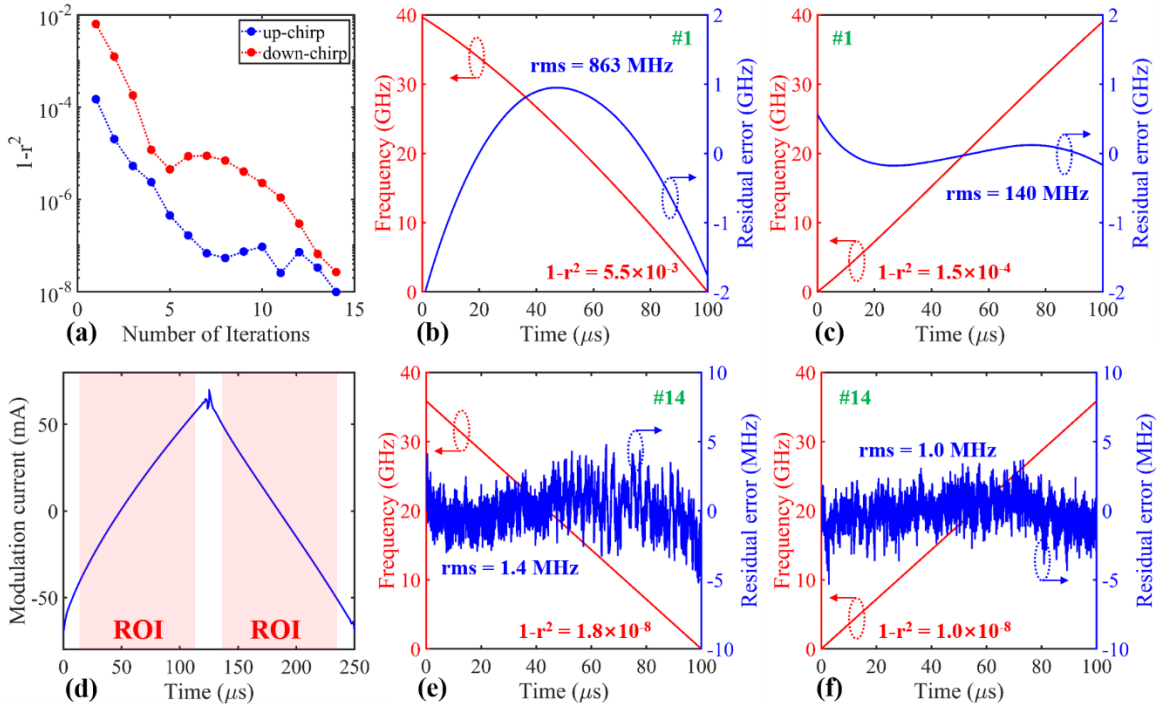


Figure 2.2. Experimental results of ILC pre-distortion linearization for a commercial DFB laser. (a) Nonlinearity reduction during the ILC pre-distortion process. (b), (c) The laser down-chirp, up-chirp, and residual nonlinearities in the ROIs at the 1st iteration. (d) The pre-distorted laser modulation waveform at the 14th iteration. (e), (f) The laser down-chirp, up-chirp and residual nonlinearities in the ROIs at the 14th iteration.

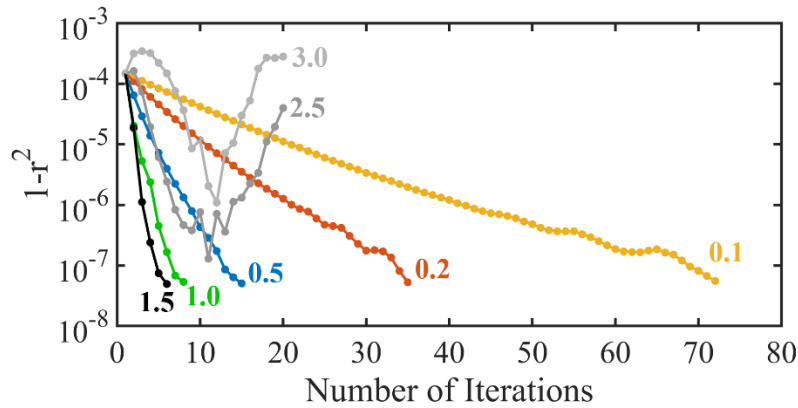


Figure 2.3. DFB laser up-chirp nonlinearity variations during the ILC pre-distortion process with different values of the p coefficient.

The ILC pre-distortion linearization is also experimentally tested on a commercial vertical-cavity surface-emitting laser (VCSEL) (RC32xxx1-FFAimst, Raycan). The laser is 3V DC biased and the pre-distorted modulation voltage waveform is superimposed on the DC bias. The setup and other configurations are the same as in the DFB laser experiments. Figure 2.4 shows the linearization results when the peak-to-peak voltage of the modulation waveform is set to 150 mV (Figure 2.4 (a) and (b)) and 500 mV (Figure 2.4 (c) and (d)). The corresponding chirp excursions are 49 GHz and 163 GHz, respectively. The relative nonlinearity after the ILC pre-distortion process is similar to that of the DFB laser, showing that the ILC pre-distortion method can be successfully applied to different types of lasers.

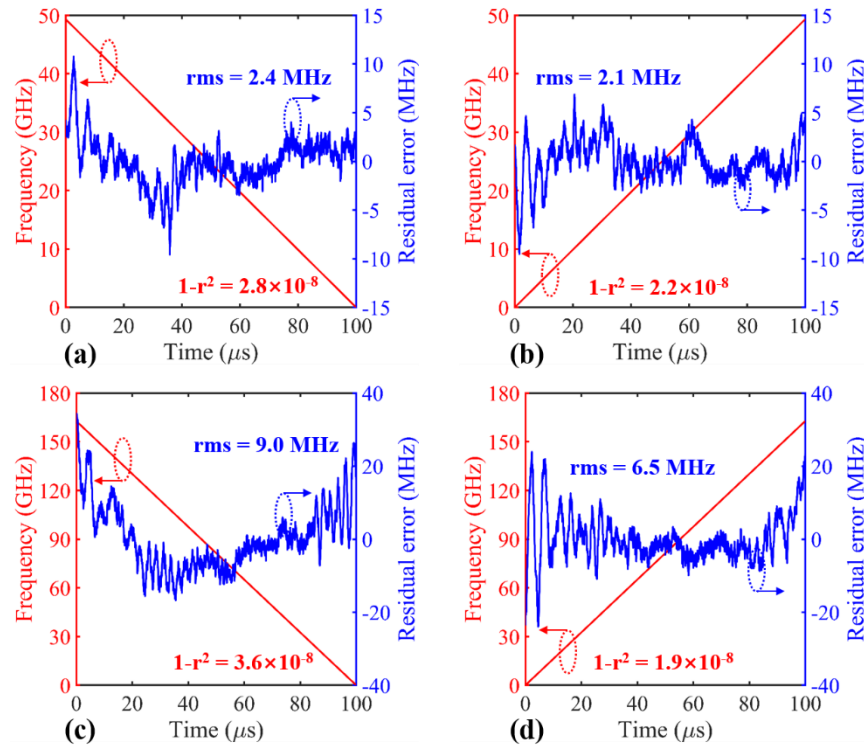


Figure 2.4. Experimental results of ILC pre-distortion linearization for a commercial VCSEL. (a), (b) The laser down-chirp, up-chirp, and residual nonlinearities after the ILC pre-distortion process for a 49 GHz chirp. (c), (d) The laser down-chirp, up-chirp, and residual nonlinearities after the ILC pre-distortion process for a 163 GHz chirp.

The DFB laser driven by the ILC pre-distorted waveform is implemented in a fiber-based monostatic FMCW LiDAR with a 25.4 mm transmitting/receiving aperture and an output power of 15 mW. The laser beam is mechanically scanned by a commercial 2-axis galvanometer mirror system (GVS012, Thorlabs) in a field of view of 24° (azimuth) \times 20° (elevation) with 0.02° increments in both axes. The beam scanner control and data processing are performed on a laptop computer. A stationary scene composed of multiple objects at approximately 3 m distance from the LiDAR is 3D imaged. Figure 2.5 shows the measured 3D point cloud composed of high-fidelity 3D images of objects such as the stack of books, the toy, the cup, the keyboard, the monitor, the wall, and the desk [8]. The results suggest the ILC pre-distortion method is able to linearize the laser chirp so that high ranging resolution can be achieved.

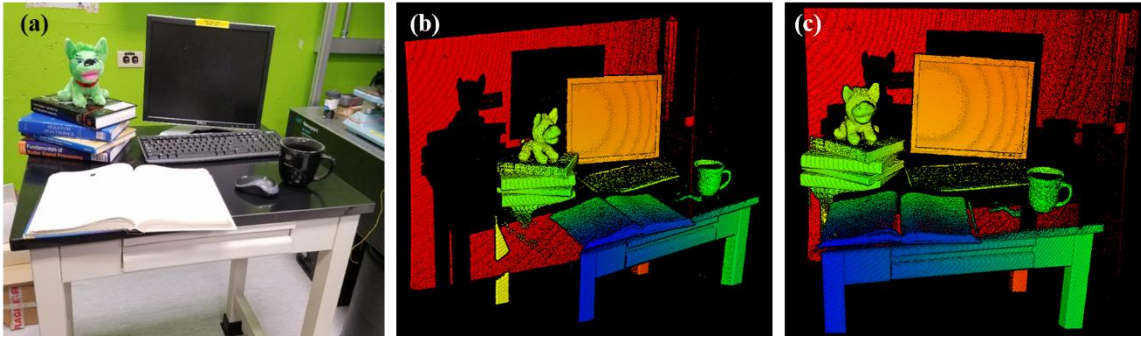


Figure 2.5. (a) Camera image of the scene (not in the same view angle of LiDAR). (b), (c) 3D point clouds (the same point cloud in two view angles) visualized by the CloudCompare software with eye-dome lighting [19]. The color of the points represents depth. [8]

3. Phase noise compensation process

3.1 Principle and setup

Although the ILC pre-distortion method can significantly reduce the systematic nonlinearity and achieve bandwidth-limited LiDAR resolution at a distance of tens of meters, random laser chirp nonlinearities due to the laser phase noise cannot be solved by

the pre-distortion method because they are not repetitive, which can degrade the LiDAR resolution at a longer distance. Therefore, real-time laser chirp measurement and phase noise compensation are required in this case.

Figure 3.1 shows a schematic of the proposed phase noise compensation process. A small portion (10%) of the laser power is tapped into a monitor MZI with a fixed time delay τ_m . This monitor MZI may be the same one used for the ILC pre-distortion process, so there is no additional setup complexity. The laser chirp can be described by $\nu(t) = \nu_0 + \gamma t + \nu_{nl}(t)$ as discussed in section 1.3, so the beat signal frequency in the monitor MZI is composed of an ideal constant term $\gamma\tau_m$ and a nonlinearity induced varying term $[\nu_{nl}(t) - \nu_{nl}(t - \tau_m)]$. Defining the optical phase noise $\varphi_n(t) = 2\pi[\nu_{nl}(t)dt]$ and the beat signal phase noise $\Delta\varphi_n(t, \tau_m) = \varphi_n(t) - \varphi_n(t - \tau_m)$, the beat signal detected by the balanced photodetectors can be represented by

$$\begin{aligned} U_m(t) &= A_m \cos[2\pi\gamma\tau_m t + \varphi_n(t) - \varphi_n(t - \tau_m)] \\ &= A_m \cos[2\pi\gamma\tau_m t + \Delta\varphi_n(t, \tau_m)], \end{aligned} \quad (3.1)$$

where A_m is the signal amplitude.

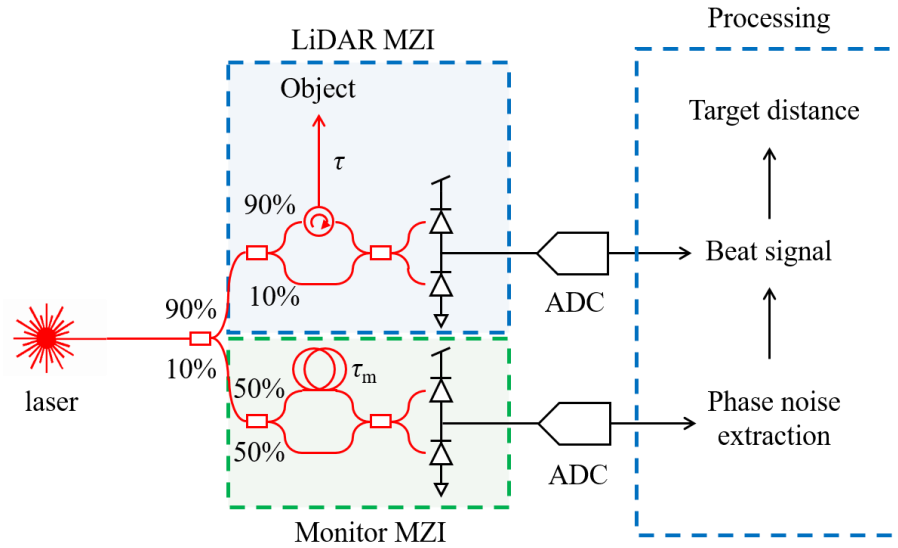


Figure 3.1. Schematic of the phase noise compensation setup and process.

Our goal is to obtain $\Delta\varphi_n(t, \tau_m)$ which contains the effects of the laser phase noise. This can be achieved by applying a Hilbert Transform (HT) to extract the phase of the beat signal in Equation (3.1) and then subtracting the known term $2\pi\gamma\tau_m t$. An accurate phase extraction by HT requires the positive-frequency and negative-frequency lobes in the double-sided spectrum of the beat signal not to overlap, i.e. the central frequency $2\pi\gamma\tau_m$ should be larger than the spectral peak broadening due to $\Delta\varphi_n(t, \tau_m)$. This suggests that to improve the HT accuracy, we prefer a large monitor MZI delay τ_m that separates the two lobes far away and a small laser chirp nonlinearity that does not broaden the spectral peak across the zero frequency. This is the reason why an ILC pre-distortion process is necessary to reduce the systematic nonlinearity before the phase noise compensation process since the initial systematic nonlinearity is typically much larger than the random nonlinearity and can degrade the HT phase extraction accuracy.

Similar to Equation (3.1), for the LiDAR MZI with an unknown object round-trip time τ and Doppler shift f_D , the beat signal is

$$\begin{aligned} U(t) &= A \cos\left[2\pi(\gamma\tau + f_D)t + \varphi_n(t) - \varphi_n(t - \tau)\right] \\ &= A \cos\left[2\pi(\gamma\tau + f_D)t + \Delta\varphi_n(t, \tau)\right]. \end{aligned} \quad (3.2)$$

If the phase noise $\Delta\varphi_n(t, \tau) = \varphi_n(t) - \varphi_n(t - \tau)$ can be computed from the measured monitor MZI phase noise $\Delta\varphi_n(t, \tau_m) = \varphi_n(t) - \varphi_n(t - \tau_m)$, the laser phase noise effects can be fully canceled out from Equation (3.2). Unfortunately, the laser phase noise $\varphi_n(t)$ cannot be uniquely solved from $\Delta\varphi_n(t, \tau_m)$, therefore $\Delta\varphi_n(t, \tau)$ for an arbitrary round-trip time τ may not be computed unambiguously. However, for some certain values of τ that are integral multiples of τ_m , i.e. $\tau = k\tau_m$ where $k = 0, 1, 2, \dots$, the phase noise $\Delta\varphi_n(t, k\tau_m)$ can be computed without ambiguity,

$$\Delta\varphi_n(t, k\tau_m) = \begin{cases} \sum_{p=0}^{k-1} \Delta\varphi_n(t - p\tau_m, \tau_m), & k \geq 1; \\ 0, & k = 0. \end{cases} \quad (3.3)$$

An arbitrary object round-trip time τ can be represented by a combination of an integral multiple of τ_m and a residual delay $\delta\tau$, i.e. $\tau = k\tau_m + \delta\tau$ where $|\delta\tau| \leq \tau_m/2$, and the phase noise can be split into two terms accordingly,

$$\Delta\varphi_n(t, \tau) = \Delta\varphi_n(t, k\tau_m + \delta\tau) = \Delta\varphi_n(t, k\tau_m) + \Delta\varphi_n(t - k\tau_m, \delta\tau), \quad (3.4)$$

where the first term $\Delta\varphi_n(t, k\tau_m)$ is known from the monitor MZI according to Equation (3.3), and the second term $\Delta\varphi_n(t - k\tau_m, \delta\tau)$ is an unknown phase noise term due to a small delay $\delta\tau$. The phase noise in the beat signal $U(t)$ can be partially compensated for by multiplying $\exp[-j\Delta\varphi_n(t, k\tau_m)]$ to $U(t)$ in Equation (3.2) during the signal processing,

$$\begin{aligned} U_k(t) &= U(t) \exp[-j\Delta\varphi_n(t, k\tau_m)] \\ &= \frac{A}{2} \left\{ \exp[j2\pi(\gamma\tau + f_D)t + j\Delta\varphi_n(t, \tau)] + \exp[-j2\pi(\gamma\tau + f_D)t - j\Delta\varphi_n(t, \tau)] \right\} \\ &\quad \cdot \exp[-j\Delta\varphi_n(t, k\tau_m)] \\ &= \frac{A}{2} \left\{ \exp[j2\pi(\gamma\tau + f_D)t + j\Delta\varphi_n(t - k\tau_m, \delta\tau)] \right. \\ &\quad \left. + \exp[-j2\pi(\gamma\tau + f_D)t - 2j\Delta\varphi_n(t, k\tau_m) - j\Delta\varphi_n(t - k\tau_m, \delta\tau)] \right\}. \end{aligned} \quad (3.5)$$

The processed signal $U_k(t)$ has an asymmetric spectrum with two lobes around frequencies $\pm(\gamma\tau + f_D)$. The phase noise in the positive lobe is reduced from $\Delta\varphi_n(t, \tau)$ with effects from the entire object round-trip time τ , to $\Delta\varphi_n(t - k\tau_m, \delta\tau)$ with effects only from the residual short delay $\delta\tau$ within the range of $\pm\tau_m/2$. In other words, although the actual object distance is $c\tau/2$, the effective distance for the phase noise is reduced to $c\delta\tau/2$, thus the resolution and signal-to-noise ratio (SNR) of this lobe is significantly enhanced according to Equation (1.5). The phase noise in the negative lobe is approximately doubled resulting in a worse resolution and SNR, but this lobe carries no extra object distance or velocity information thus can be ignored. If an in-phase/quadrature (I/Q) detection system is implemented, there will be no negative lobe in the signal spectrum. A multiplication instead of a resampling process is necessary in order to preserve the Doppler shift information and avoid the computational-heavy interpolation operations.

In practice, there is usually no prior knowledge of the object distance and velocity, thus the exact integer factor k is unknown. Therefore, all of the k values from the set of 0,

1, 2, ..., K are respectively plugged into Equations (3.3) and (3.5), where K represents the maximum k value corresponding to the detection range, resulting in a series of processed signals $U_k(t)$. The effective round-trip time in $U_k(t)$ is $|\tau - k\tau_m|$, and the one with $|\tau - k\tau_m| \leq \tau_m/2$ will have the best resolution and SNR. Figure 3.2 shows an example of a stationary object with a round-trip time τ between $3\tau_m$ and $4\tau_m$. In this example, $U_4(t)$ will have the best compensation result since the effective round-trip time of the object is the smallest.

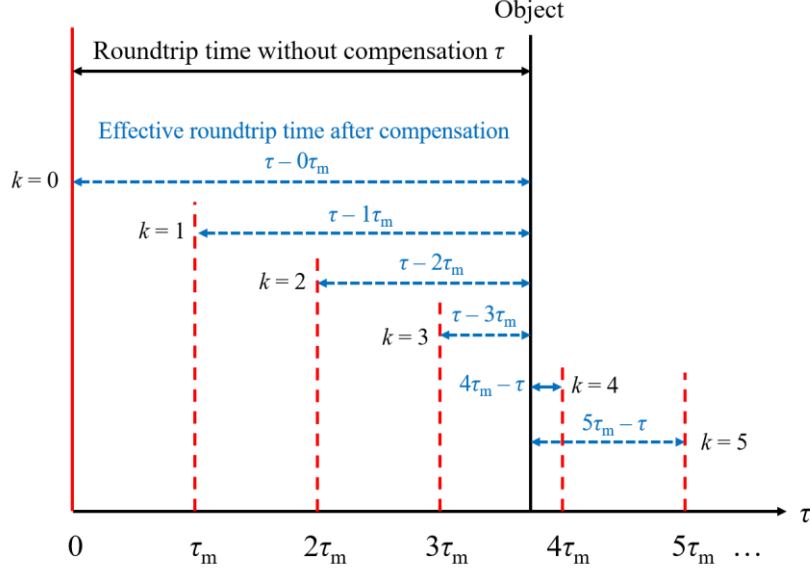


Figure 3.2. Effective round-trip time of a stationary object in the processed beat signals for different k values.

As discussed above, a large monitor MZI delay τ_m helps increase the HT phase extraction accuracy. A large τ_m also results in a small K value, i.e. the number of processed beat signals computed for each measurement, thus reduces the computational cost. However, the maximum effective round-trip time $\tau_m/2$ will be large in this case, degrading the phase noise compensation results. In practice, according to Equation (1.5), a τ_m around $1/2\pi\nu_{nl,rms}$ may be a good choice, where $\nu_{nl,rms}$ is the RMS value of the laser chirp nonlinearity due to the phase noise, so that bandwidth-limited LiDAR resolution can be achieved even with the largest effective round-trip time. If the object distance and velocity can be roughly estimated in advance, the computational cost can be further reduced by narrowing the range of k values.

The spectra, i.e. Fourier Transforms, of all the processed signals, $S_k(f) = \text{FT}[U_k(t)]$, are then used to generate a combined spectrum by picking up the maximum value from all the $S_k(f)$ at each frequency, i.e. $S(f) = \max\{S_0(f), S_1(f), \dots, S_k(f)\}$. This maximum operation assures that at each frequency f the best compensation results among all the k values is selected. Note that a maximum operation instead of a simple piecewise stitching demonstrated in [20] is necessary in order to ensure the effective delay at any frequency in $S(f)$ is within $\pm\tau_m/2$, since the Doppler effect may shift the spectral peak outside of the $\pm\gamma\tau_m/2$ neighborhood around the static beat frequency $\gamma\tau$. This combined spectrum can then be processed in the same way (for example a peak finding) as a regular beat signal spectrum to extract the distance and velocity of the object.

3.2 Experimental results

The proposed phase noise compensation method is tested on the same fiber-based LiDAR system with the commercial DFB laser after the ILC pre-distortion linearization described in section 2.2. The coherent length calculated from the measured DFB laser phase noise is 120 m, meaning the ranging resolution will significantly degrade for objects at a larger than 60 m distance. The monitor MZI and LiDAR MZI beat signals are synchronously recorded by the dual-channel ADC (PXIe-5114, National Instruments) at 250M samples per second. The data processing and instrument control are performed on a laptop computer.

First, a single-mode fiber with 160 m length is used as the LiDAR probe path, and the reflected light from the FC/APC interface at the end of the fiber acts as the object return light. The single-trip optical path length is approximately 240 m according to the refractive index $n \approx 1.5$ of the fiber. The monitor MZI has a delay $\tau_m = 100$ ns so the maximum effective round-trip time after compensation is 50 ns, corresponding to a 7.5 m single-trip distance. The DFB laser is modulated at a 20 kHz rate with a chirp excursion of 1.46 GHz in the ROI, resulting in a 10.3 cm distance resolution. The distance range is 260 m limited by the ADC sample rate. Figure 3.3 shows the comparison between the beat signal spectrum of the raw LiDAR data and the combined spectrum generated by the

phase noise compensation process. The object peak of the fiber to free-space interface reflection can be clearly observed on the spectrum after compensation, while no obvious peak can be observed on the spectrum of the raw beat signal.

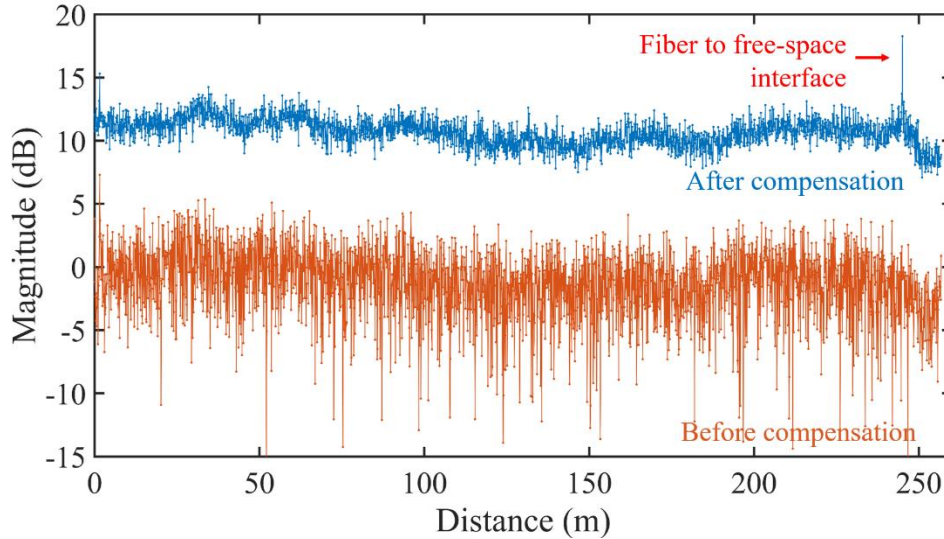


Figure 3.3. FMCW LiDAR beat signal spectra before and after phase noise compensation of an FC/APC fiber to free-space interface at 240 m distance. The plots are artificially offset for clarity.

Next, a combination of fiber and free-space paths is used as the LiDAR probe path. The fiber path is composed of three sections of single-mode fibers with 30 m, 20 m, and 6 m lengths connected by FC/APC connectors, and the corresponding optical path lengths are approximately 44 m, 30 m, and 9 m respectively. The free-space path is 40 m long and ends on a white wall, with a mirror halfway for path folding. The combined single-trip path length is 123 m. A monitor MZI delay $\tau_m = 30$ ns is used in this case for better compensation results so the maximum effective round-trip time after compensation is 15 ns, corresponding to a 2.25 m single-trip distance. The DFB laser is modulated at a 20 kHz rate with a chirp excursion of 2.49 GHz in the ROI, resulting in a 6.0 cm distance resolution and a 150 m range. Figure 3.4 shows the comparison between the beat signal spectrum of the raw LiDAR data and the combined spectrum generated by the phase noise compensation process. Spectral peaks of multiple reflection sources along the light path such as the fiber connectors, the fiber to free-space interface, the mirror scattering,

and the white wall can be observed in the processed spectrum with high resolution. The corresponding peaks in the spectrum of the raw data have significantly lower resolution and SNR.

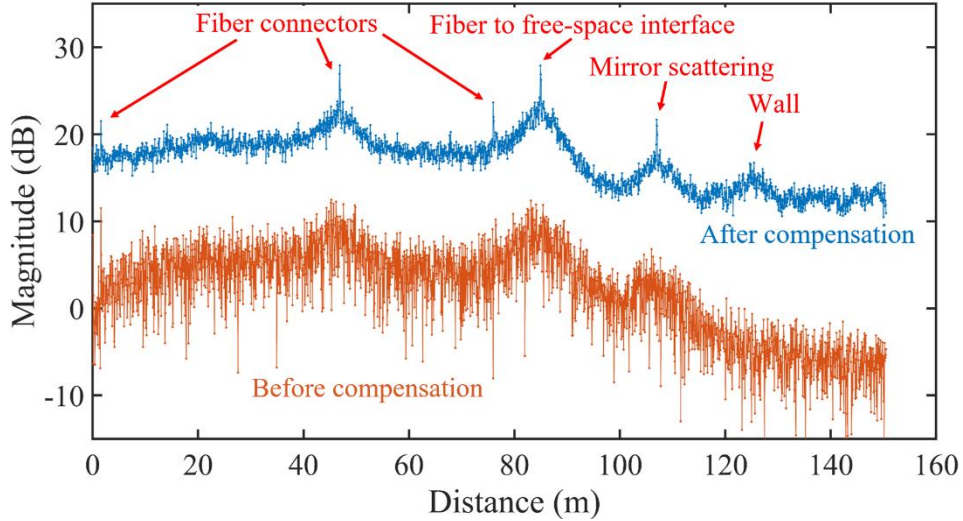


Figure 3.4. FMCW LiDAR beat signal spectra before and after phase noise compensation of a light path composed of three sections of single-mode fibers and a free-space path ending at a white wall. The plots are artificially offset for clarity.

3D imaging at long distances is then tested with the phase noise compensation process. The DFB laser modulation configuration is the same as the previous experiment. The laser beam is mechanically scanned by a commercial 2-axis galvanometer mirror system (GVS012, Thorlabs), aiming at an opened door of a room at the end of the 35 m corridor, shown in Figure 3.5 (a). The lateral scan resolution is $100 \text{ pixels} \times 200 \text{ pixels}$. A person is standing in front of the opened door as the object. To demonstrate long-distance operation, a 63 m optical path length fiber is also inserted into the light path so the overall object distance is extended to about 100 m. Figure 3.5 (b) and (c) show the measured 3D point cloud. The outline of the person is captured with high fidelity in the 3D image, while the reflectivity of clothes is higher than the reflectivity of the skin resulting in a higher SNR in the clothes area. The back wall of the room can also be seen in the point cloud. The SNR of the measurement with the 63 m extension fiber is slightly lower due to the higher optical loss of the longer path.

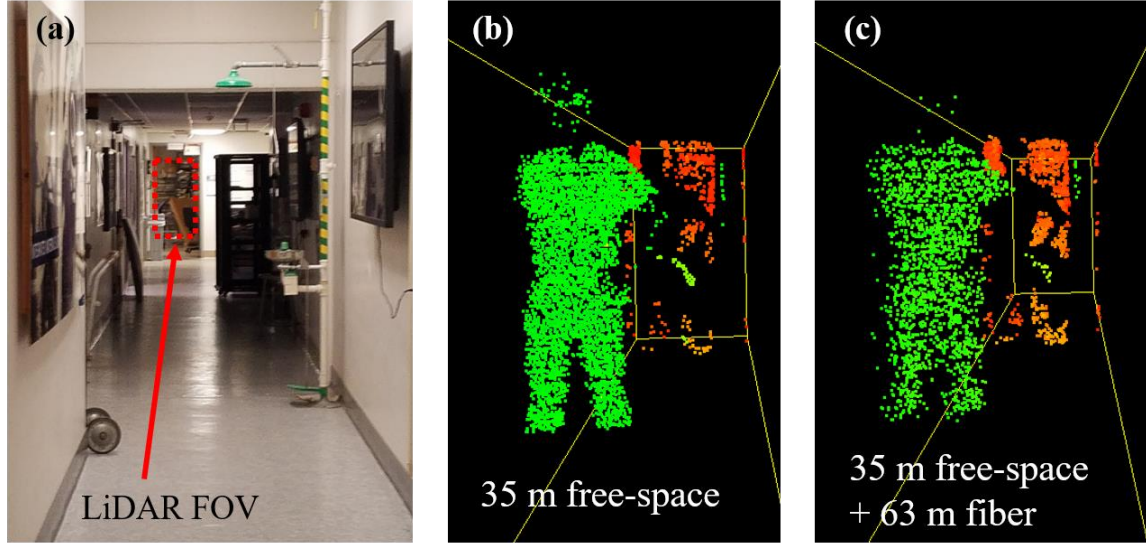


Figure 3.5. (a) Camera image showing the LiDAR light path and field of view (FOV). (b), (c) 3D point clouds measured by the FMCW LiDAR with phase noise compensation of a person standing in front of an opened door. The color of the points represents depth.

The single point and 3D imaging LiDAR experiment results suggest that the proposed post-processing phase noise compensation method is able to extend the LiDAR detection range to hundreds of meters without requiring a narrow-linewidth laser or complex linewidth suppression setup.

4. Conclusions

FMCW LiDAR is a promising 3D imaging technology with special advantages on lower power consumption, lower electronics bandwidth, intrinsic interference prevention, and velocity detection capability. However, the strict requirements on the laser chirp linearity and phase noise often become the bottleneck of simple and low-cost implementation.

In this work, we propose a two-step method for laser chirp linearization and phase noise compensation. The systematic nonlinearity of the laser chirp due to the nonlinear laser dynamics is first compensated for by the ILC pre-distortion process, achieving

bandwidth-limited resolution for objects at a short to medium range (tens of meters). The random nonlinearity, i.e. the laser phase noise, is then compensated for by the post-processing method with the help of a monitor MZI, further extending the bandwidth-limited resolution range to a long distance (hundreds of meters). In the experiments with a commercial DFB laser, a 0.003% relative chirp nonlinearity and 24 m bandwidth-limited resolution range is achieved after the ILC pre-distortion process, and a more than 250 m range is achieved after the phase noise compensation process. The proposed methods are easy to be implemented with only an additional monitor MZI, can be applied on any type of lasers, and have low computational cost. The ILC pre-distortion linearization can even be used alone for short to medium distances without any active control or additional post-processing. We believe the proposed methods open a way to low-cost and high-performance FMCW LiDAR systems.

5. Funding and Acknowledgements

This work is funded in part by the Bakar Fellows Program at UC Berkeley, and Berkeley Sensor and Actuator Center (BSAC).

I would like to first thank my advisor Professor Ming C. Wu for his insights, guidance, and supports for this project. I would like to thank Dr. Phillip Sandborn for leading me into the project as my mentor, and thank Jazz Pouls and Margaret Zhang for their help as undergraduate researchers. I would also like to thank Professor Vladimir Stojanovic for serving as the reader of this report and providing valuable suggestions.

6. References

- [1] A. O’Riordan, T. Newe, G. Dooly, and D. Toal, “Stereo Vision Sensing: Review of existing systems,” in *Proceedings of the 12th International Conference on Sensing Technology (ICST)*, (IEEE, 2018), pp. 178–184.
- [2] S. Zhang, “High-speed 3D shape measurement with structured light methods: A review,” *Optics and Lasers in Engineering* **106**, 119–131 (2018).
- [3] M. A. Richards, *Fundamentals of radar signal processing*, 2nd edition. (McGraw-Hill, 2014).
- [4] G. Allevato, J. Hinrichs, M. Rutsch, J. Adler, A. Jäger, M. Pesavento, and M. Kupnik, “Real-Time 3D Imaging using an Air-Coupled Ultrasonic Phased-Array,” *IEEE Transactions on Ultrasonics, Ferroelectrics, and Frequency Control* (2020).
- [5] B. Behroozpour, P. A. M. Sandborn, M. C. Wu, and B. E. Boser, “Lidar system architectures and circuits,” *IEEE Communications Magazine* **55**(10), 135–142 (2017).
- [6] J. C. Owens, “Optical Refractive Index of Air: Dependence on Pressure, Temperature and Composition,” *Applied Optics* **6**(1), 51–59 (1967).
- [7] E. Baumann, F. R. Giorgetta, I. Coddington, L. C. Sinclair, K. Knabe, W. C. Swann, and N. R. Newbury, “Comb-calibrated frequency-modulated continuous-wave lidar for absolute distance measurements,” *Optics Letters* **38**(12), 2026–2028 (2013).
- [8] X. Zhang, J. Pouls, and M. C. Wu, “Laser frequency sweep linearization by iterative learning pre-distortion for FMCW LiDAR,” *Optics Express* **27**(7), 9965–9974 (2019).
- [9] R. J. Pieper, “Laboratory and computer tests for Carson’s FM bandwidth rule,” in *Proceedings of the 33rd Southeastern Symposium on System Theory* (IEEE, 2001), pp. 145–149.
- [10] A. Vasilyev, “The Optoelectronic Swept-Frequency Laser and Its Applications in Ranging, Three-Dimensional Imaging, and Coherent Beam Combining of Chirped-Seed Amplifiers,” *Ph.D. Dissertation, California Institute of Technology* (2013).
- [11] J. Qin, L. Zhang, W. Xie, R. Cheng, Z. Liu, W. Wei, and Y. Dong, “Ultra-long range optical frequency domain reflectometry using a coherence-enhanced highly

- linear frequency-swept fiber laser source,” *Optics Express* **27**(14), 19359–19368 (2019).
- [12] B. Behroozpour, P. A. M. Sandborn, N. Quack, T. Seok, Y. Matsui, M. C. Wu, and B. E. Boser, “Electronicphotonic integrated circuit for 3D microimaging,” *IEEE Journal of Solid-State Circuits* **52**(1), 161–172 (2017).
- [13] P. A. M. Sandborn, T. Hariyama, and M. C. Wu, “Resolution-enhancement for wide-range non-linear FMCW lidar using quasi-synchronous resampling,” in *Imaging and Applied Optics 2017, OSA Technical Digest* (online) (Optical Society of America, 2017), paper DW3F.3.
- [14] C. J. Karlsson and F. Å. A. Olsson, “Linearization of the frequency sweep of a frequency-modulated continuouswave semiconductor laser radar and the resulting ranging performance,” *Applied Optics* **38**(15), 3376–3386 (1999).
- [15] N. Satyan, A. Vasilyev, G. Rakuljic, V. Leyva, and A. Yariv, “Precise control of broadband frequency chirps using optoelectronic feedback,” *Optics Express* **17**(18), 15991–15999 (2009).
- [16] J. Zhang, J. Wang, M. Xu, F. Lu, L. Chen, J. Yu, and G. Chang, “Memory-polynomial digital pre-distortion for linearity improvement of directly-modulated multi-IF-over-fiber LTE mobile fronthaul,” in *Proceedings of IEEE Optical Fiber Communications Conference and Exhibition* (IEEE, 2016), paper TU2B.3.
- [17] H. Ahn, Y. Chen, and K. L. Moore, “Iterative learning control: Brief survey and categorization,” *IEEE Transactions on Systems, Man, and Cybernetics, Part C* **37**(6), 1099–1121 (2007).
- [18] J. Chani-Cahuana, P. N. Landin, C. Fager, and T. Eriksson, “Iterative learning control for RF power amplifier linearization,” *IEEE Transactions on Microwave Theory and Techniques* **64**(9), 2778–2789 (2016).
- [19] C. Boucheny and A. Ribes, “Eye-dome lighting: a non-photorealistic shading technique,” *Kitware Source Quarterly Magazine* **17** (Kitware Blog, 2011).
<https://blog.kitware.com/eye-dome-lighting-a-non-photorealistic-shading-technique/>.

- [20] F. Ito, X. Fan, and Y. Koshikiya, "Long-Range Coherent OFDR With Light Source Phase Noise Compensation," *IEEE Journal of Lightwave Technology* **30**(8), 1015–1024 (2012).